



# Efficiency of pulse pumped soliton microcombs

JIANG LI,<sup>1,2,†</sup> CHENGYING BAO,<sup>1,3,†</sup> QING-XIN JI,<sup>1,†</sup> HEMING WANG,<sup>1</sup> LUE WU,<sup>1</sup> STEPHANIE LEIFER,<sup>4</sup> CHARLES BEICHMAN,<sup>4</sup> AND KERRY VAHALA<sup>1,\*</sup>

<sup>1</sup>T. J. Watson Laboratory of Applied Physics, California Institute of Technology, Pasadena, California 91125, USA

<sup>2</sup>Current address: hQphotonics Inc., 2500 E Colorado Blvd., Pasadena, California 91107, USA

<sup>3</sup>Current address: State Key Laboratory of Precision Measurement Technology and Instruments, Department of Precision Instruments, Tsinghua University, Beijing 100084, China

<sup>4</sup>Jet Propulsion Laboratory, 4800 Oak Grove Drive, Pasadena, California 91109, USA

\*Corresponding author: vahala@caltech.edu

Received 14 September 2021; revised 28 January 2022; accepted 1 February 2022 (Doc. ID 443060); published 18 February 2022

**Temporal soliton mode locking in coherently pumped microcavities is a promising route towards miniaturized frequency comb systems. However, the power efficiency of the resulting microcombs is usually quite low. Soliton generation by pulse pumping provides a way to increase conversion efficiency (so far, as high as 8%). Here, we study conversion efficiency and report a single-soliton conversion efficiency as high as 54% using a scanning laser, as well as a steady-state single-soliton conversion efficiency as high as 34%. We use the Lagrangian approach to develop analytical expressions for efficiency and soliton temporal placement within the pumping pulse, and our measurements reveal features in the tuning dependence of soliton power and efficiency not seen in continuous pumping. Our experimentally confirmed expressions for efficiency will be useful in understanding advantages and limitations of pulse pumped systems.** © 2022 Optical Society of America under the terms of the [OSA Open Access Publishing Agreement](https://doi.org/10.1364/OPTICA.443060)

<https://doi.org/10.1364/OPTICA.443060>

## 1. INTRODUCTION

Soliton mode locking in optical microresonators provides chip-scale frequency combs at microwave to terahertz repetition rates [1,2]. These microcombs can ultimately reduce the size, weight, and power consumption of conventional frequency comb systems. They have been applied across numerous applications including optical frequency synthesis [3], spectroscopy [4,5], astrocombs [6,7], and optical communication [8,9]. An undesirable feature of soliton microcombs is their low continuous wave (cw) pumping efficiency [10–13]. A simple analysis shows that the maximum cw pumping efficiency (soliton power divided by input pump power) of soliton microcombs is given by [11,14]

$$\Gamma^{\text{cw}} = 2\pi^2 \eta^2 \frac{\tau_s}{T_R}, \quad (1)$$

where  $\tau_s$  is the soliton pulse width,  $T_R$  is the cavity round-trip time, and  $\eta \equiv Q/Q_{\text{ex}}$  is the resonator loading factor, with  $Q$  and  $Q_{\text{ex}}$  being the total and external Q factors ( $Q^{-1} = Q_0^{-1} + Q_{\text{ex}}^{-1}$ , where  $Q_0$  is the intrinsic Q factor).  $\Gamma^{\text{cw}}$  results from operation at maximum possible pump detuning (maximum soliton power) or equivalently minimum possible pumping power for a given pump detuning (see Ref. [11] and Supplement 1, Section 6). Since  $\eta$  is at most unity, this result makes clear that efficiency varies like  $\tau_s/T_R$ , a scaling that has restricted bright soliton efficiency to the 1% range. While non-bright soliton microcombs can have a much higher conversion efficiency (up to 49%) [15–18], these normal dispersion microcombs have so far operated with relatively narrow comb bandwidth, and their larger duty-cycle makes amplification

to high peak power challenging. Other more complicated schemes, such as coupled dual cavities, have also been proposed to enhance the conversion efficiency of cw pumped bright soliton microcombs [19]. The interplay between  $\chi^{(2)}$  and  $\chi^{(3)}$  effects in an AlN microcavity was also used to reach a conversion efficiency of 17% for solitons [20].

Pulse pumping of microcavities offers a straightforward way to increase pumping efficiency [21]. Solitons are generated by a periodic pulsed pump instead of a continuous pump, and this pumping scheme has been receiving increasing interest in recent years [7,21–25]. Improved efficiency results because the soliton resides under a pump pulse profile having a significantly higher peak power than the average power of the pump pulse. Using this method, a 5% soliton conversion efficiency was measured by pumping a monolithic fiber Fabry–Perot (FP) resonator with 2 ps pulses at 9.8 GHz repetition rate [21]. A silicon-nitride microcomb at a detectable repetition rate (28 GHz line spacing) was also demonstrated to have a conversion efficiency of 8% [22]. The same device, when operated with nearly an octave span, achieved an efficiency of 2.8%. The latter result is particularly significant since detectable rate operation at octave span facilitates comb self-referencing [26], while at the same time this combination of features (large  $T_R$  and small  $\tau_s$ ) causes very low efficiency for continuous pumping [see Eq. (1)]. Pulsed pumping also overcomes microcomb designs featuring relatively larger  $V/Q^2$  ( $V$  is mode volume), which sets the scaling of the parametric threshold [7,24]. As additional benefits of pulse pumping, the generated soliton repetition rate is locked to the pumping repetition rate, thereby obviating stabilization of

the repetition rate [21], and suppression of noise transfer from the pump pulse repetition rate to the soliton repetition rate has been observed [22,23]. Pulse pumping has also been used for discrete tuning of the comb line spacing by application of a pump rate that is a rational harmonic of the cavity free-spectral-range [24]. Finally, it provides additional parameters (e.g., pump repetition rate, pump pulse width, and chirp) to manipulate soliton states and study their underlying physics, including spontaneous symmetry breaking [27] and soliton tweezing [28].

In this paper, we study soliton generation in a picosecond pulse pumped silica wedge microcavity [29]. With strong over-coupling of the cavity, single-soliton operation with steady-state conversion efficiency up to 34% is attained using 2 ps pump pulses, while a transient efficiency up to 54% is measured using 1 ps pump pulses under frequency-scanning conditions. These values are conservatively measured by omitting comb lines that lie at pump frequencies. The Lagrangian method is used to develop analytical expressions for soliton power efficiency as well as relative temporal location of the soliton and pumping pulse in the cavity. These results are compared with simulation and experiment and show the importance of the Raman process in controlling power transfer efficiency.

## 2. POWER AND EFFICIENCY

Under conditions of pulse pumping, assume that the input pump power is given by  $P(t)$  such that  $t = 0$  corresponds to the pump-pulse maximum. A soliton having pulse width much narrower than the pumping pulse would therefore experience an average local pumping power  $P(t_s)$ , where  $t_s$  is the temporal location of the soliton pulse in the resonator relative to a pump pulse maximum [see Fig. 1(a)]. A Lagrangian analysis presented in Sections 3 and 4 of Supplement 1 shows that the soliton power is given by the expression

$$P_s = \frac{2\omega_0}{g'Q_{\text{ex}}}\sqrt{\frac{D_2\omega_0}{D_1^2Q}}\xi^{1/2}\left[1 + \frac{2}{\xi^{3/2}}\sqrt{\xi_0(t_s) - \xi}\right], \quad (2)$$

where  $D_1 = 2\pi/T_R$ ,  $D_2$  is the second-order dispersion (i.e., mode  $\mu$  has a frequency  $\omega_\mu = \omega_0 + D_1\mu + D_2\mu^2/2$ ), and  $g' = \omega_0 n_2 / A_{\text{eff}} n_0$  is the nonlinear coupling parameter with  $n_2$  the Kerr coefficient,  $n_0$  the refractive index, and  $A_{\text{eff}}$  the mode effective area. Also, the normalized pump detuning is defined as  $\xi \equiv 2Q\delta\omega/\omega_0$  with  $\delta\omega \equiv \omega_0 - \omega_p$  ( $\omega_p$  and  $\omega_0$  are the pumping frequency and resonator frequency that are pumped), and  $\xi_0(t_s)$  is given by

$$\xi_0(t_s) = \frac{\pi^2}{8} \frac{P(t_s)}{P_{\text{th}}}, \quad (3)$$

where  $P_{\text{th}} = \omega_0^2 T_R / (8g'\eta Q^2)$  is the parametric oscillation threshold pumping power [11]. For convenience in the theoretical analysis, we calculated the output power based on a sech-pulse shape in the time domain, which means that power in the pump frequencies within the sech<sup>2</sup> spectral envelope is included in Eq. (2). However, power carried by the pump frequencies was not included when calculating the measured efficiencies (see Sections 3.A and 3.B). This means that measured efficiencies are expected to be lower than for theory. Overall, it is interesting to note that the form of Eq. (2) is similar to a version derived for cw pumping [30], but with the important difference that  $\xi_0(t_s)$  depends upon the

location,  $t_s$ , of the soliton relative to the pumping pulse. In effect, the Lagrangian analysis shows that the soliton experiences a local pump field provided that the pumping pulse is temporally wider than the soliton (which is an assumption of the analysis).

The pumping efficiency (soliton power divided by averaged pulsed input power) is given by the following expression:

$$\begin{aligned} \Gamma^{\text{pulse}} &= 2\pi^2\eta^2 \frac{\tau_s(\xi)}{\tau_p} \frac{\xi}{\xi_0(0)} \left[1 + \frac{5}{2\xi^{3/2}}\sqrt{\xi_0(t_s) - \xi}\right] \\ &= \frac{\omega_0}{\pi g'Q_{\text{ex}}} \frac{\sqrt{2D_2\delta\omega}}{P_0} \frac{T_R^2}{\tau_p} \left[1 + \frac{2}{\xi^{3/2}}\sqrt{\xi_0(t_s) - \xi}\right], \quad (4) \end{aligned}$$

where a pump pulse power given by  $P(t) = P_0 \text{Sinc}^2(\pi t/\tau_p)$  has been assumed ( $\tau_p$  characterizes the pump pulse width). This temporal profile is close to the form generated in this work using an electro-optic (EO) comb, and it results in an average input power of  $P_{\text{avg}} = P_0\tau_p/T_R$ , where a pumping rate close to  $1/T_R$  is assumed. In the first line, Eq. (4) has been written in a way to allow better comparison with Eq. (1) giving the cw efficiency. Here, it can be seen that the leading order form of both equations is similar (note: Eq. (1) gives the maximum possible efficiency in the cw case, which occurs at  $\xi = \xi_0$ ). However, in the pulse pumping efficiency, the soliton pulse width  $\tau_s$  is normalized by the pumping pulse width  $\tau_p$  as opposed to the cavity round-trip time  $T_R$ . It is this modification that is primarily responsible for most of the efficiency boost provided by pulse pumping. The extra higher-order correction term appearing in Eq. (4) [and a similar correction in Eq. (2)] is needed to account for the increased pumping power that is possible under pulse pumping conditions.

The Lagrangian analysis also shows that the soliton location  $t_s$  (which enters the efficiency through  $\xi_0(t_s)$ ) is a function of pumping repetition rate  $\omega_{\text{rep}}$  and  $\xi$  through the following generalized Adler equation [31]:

$$\delta\omega_{\text{rep}} = \frac{D_2}{D_1}\Omega_{\text{Raman}}(t_s, \xi) - K_L(t_s, \xi), \quad (5)$$

where  $\delta\omega_{\text{rep}} \equiv \omega_{\text{rep}} - D_1$  is the detuning of the pumping rate  $\omega_{\text{rep}}$  relative to  $D_1$ , and  $\Omega_{\text{Raman}}$  is the Raman self-frequency shift [14]. Also,  $K_L(t_s, \xi)$  is given by

$$\begin{aligned} K_L(t_s, \xi) &= \frac{\pi D_2}{2D_1} \sqrt{\frac{g'Q\xi}{\omega_0}} \text{Re} \left[ \frac{\partial A_b^*}{\partial t_s} e^{i\varphi_s} \right] \\ &\times \left[ 1 + \frac{5}{4\xi^{3/2}}\sqrt{\xi_0(t_s) - \xi} \right], \quad (6) \end{aligned}$$

where  $A_b$  is the background field, and  $\varphi_s$  is the phase of the soliton.  $A_b$  is normalized so that  $|A_b|^2$  gives the intracavity background power associated with the pumping field. Equation (5) determines  $t_s$  upon specification of  $\delta\omega_{\text{rep}}$ ,  $\xi$ , and the pumping field profile. Significantly, the local slope of the pumping pulse (i.e.,  $\partial A_b^*/\partial t_s$ ) at the soliton location figures prominently in determination of  $t_s$ . This also elucidates the symmetry breaking for solitons trapped by a nonuniform background in the presence of Raman effects, which was numerically studied in Ref. [32]. In addition, the Lagrangian analysis gives the following result:

$$\delta\Omega = \frac{D_1\delta\omega_{\text{rep}}}{D_2}, \quad (7)$$

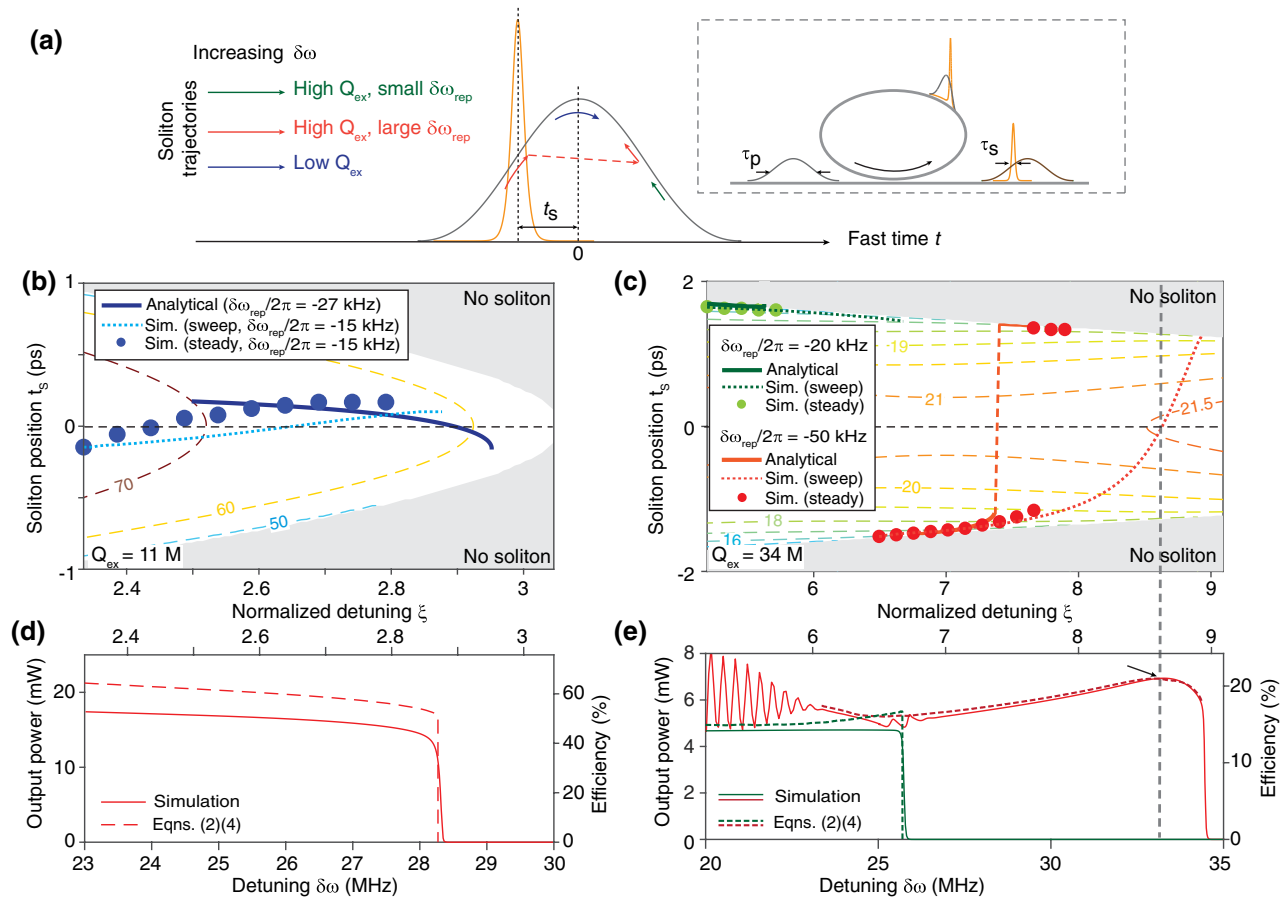


**Fig. 1.** Pulse pumped microcavity soliton. (a) Pulse pumping of a microcavity soliton in the presence of the Raman effect. Main panel: illustration of soliton position relative to the pump pulse under different pump rates and detunings. Inset: a relatively broad pumping pulse (width  $\tau_p$ ) is coupled into a microcavity. A narrower soliton pulse (width  $\tau_s$ ) is generated and trapped by the pump field. (b) Analytical efficiency iso-contours (dashed colored curves, in units of percent) versus soliton position and normalized pump detuning for  $Q_{ex} = 11$  million. Also shown are analytical [Eq. (5)] and numerically simulated soliton positions for the pump-rate detunings indicated. The dotted lines and points use the same parameters except that the dotted lines correspond to scanning of the pump detuning (i.e., non-steady state). The analysis assumes a 2 ps (FWHM width) pump pulse and  $Q_0 = 95$  million. (c) Analytical efficiency iso-contours for  $Q_{ex} = 34$  million. Also shown are analytical [Eq. (5)] and numerically simulated soliton positions for the pump-rate detunings indicated. The soliton jump is indicated by the vertical dashed red line. (d) Analytical and simulated soliton power (efficiency) versus (normalized) detuning  $\delta\omega$  ( $\xi$ ) for  $Q_{ex} = 11$  million. (e) Analytical and simulated soliton power (efficiency) versus (normalized) detuning  $\delta\omega$  ( $\xi$ ) for  $Q_{ex} = 34$  million at two different pump rates. Soliton power can reach an extremum when overlapping the pump pulse center (see arrow and vertical dashed line). The oscillations in the red solid line are attributed to breather solitons.

where  $\delta\Omega$  is the frequency shift of the soliton spectral center relative to the pump frequency. In contrast to cw pumping, this result shows that the soliton spectral center does not shift with changes in  $\xi$  (i.e.,  $\delta\omega$ ) and instead is locked by the pump repetition rate.

To understand the implications of Eq. (4) for optimally efficient operation, Fig. 1(a) provides a visualization of the soliton trajectory with respect to the pumping pulse as  $\delta\omega$  is increased. Trajectories are illustrated for two pump repetition rates that are detuned increasingly negative relative to the cavity round-trip rate. As an aside, theoretically, positive pumping-rate detuning is made difficult on account of the Raman contribution in Eq. (5), but it could not be confirmed experimentally because of challenges in accurate absolute determination of  $D_1$ . With a relatively high  $Q_{ex}$  and beginning with a pump repetition rate that is only slightly negatively detuned (green curve), the soliton is initially on the trailing edge of the pumping pulse (positive  $t_s$ ) and progresses towards the center of the pumping pulse with increasing detuning  $\delta\omega$ . Its advancement, however, is limited such that the soliton never resides at the pump maximum. Numerical studies of pulse

pumped operation have also shown that the soliton does not always sit atop the peak of the pump pulse [27]. Next, if  $\delta\omega_{rep}$  is set more negative for the high  $Q_{ex}$  case, then the situation changes, and the soliton is initially positioned on the leading edge of the pumping pulse (red curve). It then advances towards the pump maximum with increasing  $\delta\omega$ , but again never reaches the maximum and instead jumps to the trailing edge, where it then advances towards the pump pulse maximum. Finally, consider a low  $Q_{ex}$  case (dark blue curve). Subject to proper pump rate detuning, the soliton can cross and sit atop the pulse center. This is consistent with a previous numerical report that the soliton sits atop the pump pulse center with relative low peak power [27]. Further analysis based on the Lagrangian method shows that this occurs in the present case as a result of Kerr-induced modification of the phase by the pumping pulse (see Supplement 1, Section 3, where a discussion about the soliton trapping stability is also included). An approximate expression for the critical  $Q_{ex}$  that allows stable trapping of a soliton atop the pump pulse is also included in Supplement 1, Section 3.

Quantitative representation of this process is provided in Figs. 1(b) and 1(c), where soliton iso-efficiency contours are plotted versus normalized detuning  $\xi$  and  $t_s$  using Eq. (4). The contours show that operation near the pumping pulse maximum ( $t_s = 0$ ) is preferred for higher power and efficiency. Soliton trajectories are plotted for lower  $Q_{\text{ex}}$  in Fig. 1(b) and higher  $Q_{\text{ex}}$  in Fig. 1(c) cases. These are calculated using the analytical result [Eq. (5)] as well as with numerical simulations using the generalized Lugiato–Lefever equation (LLE, see Supplement 1, Sections 2 and 3) [32,33]. The numerically simulated trajectories are presented for steady state and temporal sweeping of  $\delta\omega$ . The swept case simulation allows the soliton to transiently occupy regions of higher soliton power. These transient trajectories and their associated higher efficiency (and power) operation are observable in the measurement as discussed below. Overall, for the higher  $Q_{\text{ex}}$  case, trajectories associated with more negative  $\delta\omega_{\text{rep}}$  attain better efficiency. Interestingly, this occurs for a specific  $\delta\omega$  that is not at the maximum allowable detuning. For the lower  $Q_{\text{ex}}$  case, steady trapping atop the pump pulse becomes feasible, which results in a higher efficiency. In this case, the allowable  $\delta\omega_{\text{rep}}$  to generate a soliton becomes limited, which is different from the high  $Q_{\text{ex}}$  case, where two cases of  $\delta\omega_{\text{rep}}$  are considered.

Overall, the steady-state simulated trajectories are in reasonable agreement with the analytical prediction (also steady state). However, a discrepancy in these trajectories occurs at the soliton hop location in the higher  $Q_{\text{ex}}$  case. Also, there is a discrepancy in the lower  $Q_{\text{ex}}$  case that required adjustment of the pump-rate detuning. These are believed to result from approximations used in the analytical derivation, especially for Eq. (5), which is responsible for determination of  $t_s$ . The numerically simulated and analytical results are further compared in Fig. 1(d) (lower  $Q_{\text{ex}}$ ) and Fig. 1(e) (higher  $Q_{\text{ex}}$ ), where efficiency and power are plotted versus detuning  $\delta\omega$  and normalized detuning  $\xi$ . The simulated plots are performed in the swept mode. The analytical results use Eqs. (2) and (4) for soliton power and efficiency, but with the  $t_s$  obtained from the simulation. Simulated (solid) and analytical (dashed) results are in reasonably good agreement. For the lower  $Q_{\text{ex}}$  case in Fig. 1(d), the normalized detuning  $\xi$  supporting solitons is relatively small, and the correction factor in Eqs. (2) and (5) is therefore significant. As a result, the soliton power and efficiency decrease monotonically as the detuning increases. This is in strong contrast to cw pumping, where soliton power monotonically increases with detuning. On the other hand, the higher  $Q_{\text{ex}}$  case in Fig. 1(e) shows power and efficiency that initially increase. For the more negative pump-rate detuning (red curve,  $\delta\omega_{\text{rep}}/2\pi = -50$  kHz), power and efficiency are maximum before reaching the detuning range limit. From comparison with Fig. 1(c), this corresponds to the soliton transiting across the pump pulse maximum. For the less negative pump-rate detuning (green curve,  $\delta\omega_{\text{rep}}/2\pi = -20$  kHz), the soliton remains on the trailing edge of the pumping pulse, and the attainable soliton power and efficiency are lower.

An interesting feature of the soliton jump between the leading edge and the trailing edge of the pumping pulse is a hysteresis behavior (see Supplement 1, Section 3). This results from the change in slope of the pumping pulse, which enters through Eq. (5) and abruptly switches sign upon the soliton jump. The hysteresis manifests itself by the soliton not retracing its trajectory upon increase and decrease of  $\delta\omega$ . The behavior was not observable in measurement, as it occurs where soliton power decreases with

increasing tuning. This makes servo control of the soliton difficult as discussed below.

For soliton generation to be possible, it is necessary that  $\xi_0(t_s) > \sqrt{3}$  [1,34] and therefore  $P(t_s) > 8\sqrt{3}P_{\text{th}}/\pi^2$  [from Eq. (3)]. For cw pumping, this has required careful attention to high  $Q$  resonator designs so as to maintain low enough  $P_{\text{th}}$ , especially in low repetition-rate designs, where the pumping volume is large [35]. However, the higher peak power available with pulse pumping accommodates lower  $Q$  designs so that, once a suitable pumping threshold has been achieved, only proper tuning control of the pumping laser is required for optimization of  $\xi(t_s)$  per Eq. (5). Moreover, Eq. (4) illustrates how pulse pumping somewhat decouples from efficiency the repetition-rate considerations that are manifest in Eq. (1) under cw pumping. For  $\xi(t_s)/\xi_0 = 1$ , it simplifies to the following form:

$$\Gamma^{\text{pulse}} = 2\pi^2\eta^2\tau_s/\tau_p. \quad (8)$$

This form, while not reflecting the maximum efficiency [which, as shown above, occurs for  $\xi(t_s) < \xi_0$ ] is nonetheless close in value and can serve as a convenient way to estimate efficiency. For the pump temporal profile assumed here [i.e., EO comb generated  $P(t) = P_0\text{Sinc}^2(\pi t/\tau_p)$ ], we also have  $\tau_p = T_R/N$ , where  $N$  is the number of spectral lines in the pump, and where pumping close to the round-trip rate of the microcomb is assumed. In this case, the pump line number  $N$  gives a simple estimation of the maximum efficiency that takes on the form

$$\Gamma^{\text{pulse}} = N\Gamma^{\text{cw}}. \quad (9)$$

As a caution, however, the validity of Eq. (4) [and hence also Eqs. (8) and (9)] is in question when the pump pulse width approaches the soliton pulse width. In this case, the calculated  $\Gamma$  can be non-physical (i.e., soliton power larger than pump power). This problem is explored in Supplement 1, Sections 4 and 5 and is shown to result from omission of coherent interference between the intracavity field and the transmitted pump. In the numerical simulations presented there, the highest achievable soliton conversion efficiency is 76%.

## 3. RESULTS

### A. Operation of Pulse Pumped Silica Microcomb

Figure 2(a) shows the experimental setup. The silica microcavity has  $D_1/2\pi$  (equivalent to the free-spectral-range at the mode  $\mu = 0$ ) of 22.1 GHz and  $Q_0 \sim 100$  million. The microcavity is coupled by a tapered fiber [36,37], which enables variation of the coupling conditions. The pump source is an EO comb comprised of one or two phase modulators and one intensity modulator. By compensating the phase chirp and controlling the bandwidth of the EO comb using a pulse shaper, 4 ps, 2 ps pulse, and 1 ps full-width-half-maximum pulse widths can be obtained from EO-combs containing  $N = 7, 15,$  and  $31$  comb lines, respectively. [In addition to pulse width, the number of pump lines  $N$  will be given for comparison to Eq. (9)]. The 31-line comb used two phase modulators. The EO-comb repetition rate is approximately matched to  $1/T_R$ , and soliton formation occurs by scanning the pump laser from the blue side of a cavity resonance to the red side. With the pump frequencies filtered by a wavelength division multiplexer, a soliton step can be observed during laser scanning [Fig. 2(b)]. Although the transient nonlinear thermal effects in laser scanning

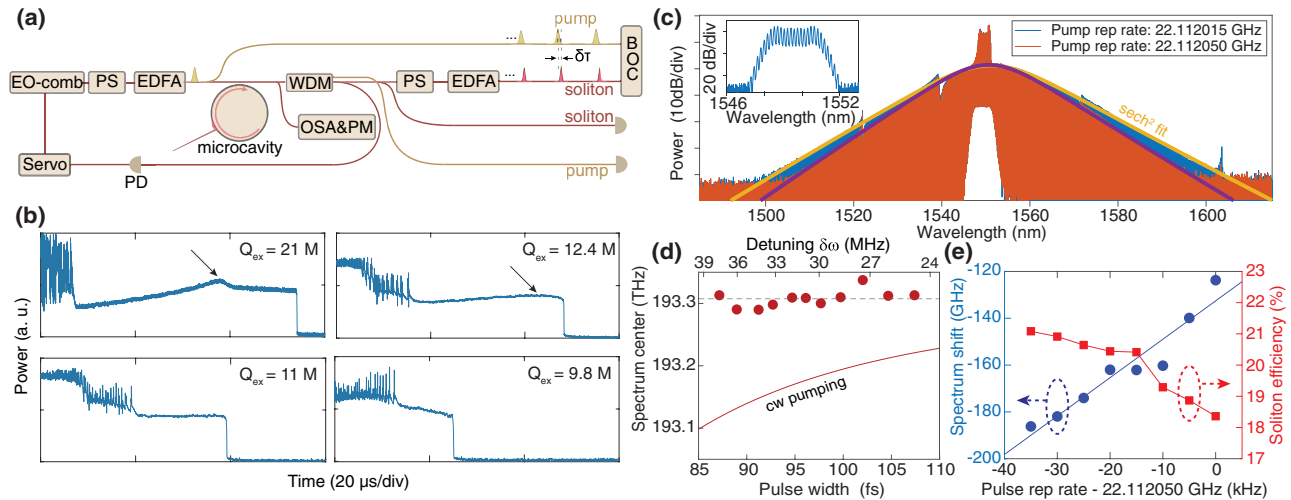


**Fig. 2.** Operation of the pulse pumped microcavity soliton. (a) Experimental setup showing an electro-optical (EO) comb used to generate pump pulses with repetition rates that closely match the free-spectral-range (22.112 GHz) of the microdisk resonator. The center frequency of the pump pulse was swept across the microcavity resonance from blue to red detuning to trigger soliton formation. The soliton comb power was detected and used to stabilize the solitons. A wavelength division multiplexer (WDM) was used to separate the pump comb lines and the soliton comb lines. A balanced optical cross-correlator (BOC) was used to measure temporal delay between the pump pulse and the soliton. PS, pulse shaper; EDFA, erbium-doped fiber amplifier; PM, power meter; PD, photodetector. (b) Measured soliton step when scanning the EO comb seed laser frequency under different cavity loadings (given by  $Q_{ex}$ ). The black arrow indicates the power maximum when the soliton crosses the pumping pulse center. No power extremum is observed, and the comb power monotonically decreases for the strong over-coupling case, e.g.,  $Q_{ex} = 9.8$  million. (c) Optical spectra and their  $sech^2$  fits of the generated microcavity solitons measured with  $Q_{ex} = 20.7$  million. Pulse pump repetition rates are 22.112015 and 22.112050 GHz, respectively. An EO comb spectrum is shown in the inset. (d) Measured soliton spectral center (red dots) plotted versus soliton pulse width (varied by change of pump frequency detuning). The solid red line is the theoretical Raman self-shift for cw pumping. (e) Spectral center frequency of the soliton (left axis) and pumping efficiency (right axis) plotted versus repetition rate of the pump pulse. The linear fit (blue) uses Eq. (7).

complicate a quantitative comparison with the theory, the measured soliton steps qualitatively agree with the theoretical analysis in Fig. 1. For example, there is an extremum within the soliton step when  $Q_{ex}$  is relatively high [see arrows in Fig. 2(b)], while no such power extremum is observed for the strongly over-coupled cases, e.g.,  $Q_{ex} = 9.8$  million. In the latter case, the comb power is monotonically decreasing with increasing laser-resonance detuning as theory predicts. It is also noted that for the  $Q_{ex} = 9.8$  M case the soliton step becomes short, which is a result of the reduced possible detuning range.

Solitons are stabilized by detection of the comb power and servo control of the laser frequency [38]. The EO-comb optical spectrum produced using one phase modulator is shown in the inset of Fig. 2(c), comprising 15 comb lines. Single-soliton spectra using an average pumping power of 25 mW are shown at two pumping rates in Fig. 2(c). The stabilized solitons feature a  $sech^2$  spectral envelope. In Fig. 2(c), the  $Q_{ex} = 20.7$  million, and the efficiency is approximately 18% and 21% for the corresponding microcombs, i.e., upper and lower efficiency points in Fig. 2(e).

As predicted by Eq. (7), the spectral center frequency of pulse pumped solitons [determined by fitting of the  $sech^2$  soliton spectrum such as shown in Fig. 2(c)] is nearly unchanged when varying the pump detuning, as shown in Fig. 2(d). This behavior is also in contrast to continuous pumping in silica resonators, where the presence of broad Raman gain causes a considerable red shift due to the Raman effect [14,39]. For comparison, the solid line in Fig. 2(d) gives the Raman soliton self-frequency shift under cw pumping based on the theory in Ref. [14]. In the experiments, the pump detuning  $\delta\omega$  [upper x axis in Fig. 2(d)] was adjusted by the locking power level of the servo [38] and was estimated as  $\delta\omega = D_2/(2D_1^2\tau_s^2)$ , with  $\tau_s$  determined from the soliton spectral

bandwidth. A spectral center frequency shift such as that caused by the Raman effect induces a change in the soliton round-trip time (and repetition rate) as a result of group velocity dispersion [14,40]. Because pulse pumping enforces a fixed repetition rate, the spectral center frequency shift is suppressed.

On the other hand, a change in the pumping pulse repetition rate will induce a shift in the soliton spectral center, as the soliton adjusts its round-trip time to accommodate the pumping rate using dispersion [21]. In this measurement, the soliton can be generated at repetition rates ranging between 22.112050 and 22.112015 GHz [see Fig. 2(c)]. Beyond this tuning range (35 kHz), the soliton fell out of lock with the pump. By fitting several spectra between these rate limits, the soliton spectral center is plotted versus pumping rate in Fig. 2(e) (blue points). From Eq. (7) above, the measured slope of this linear shift can be used to infer  $D_2$  with knowledge of  $D_1$  (approximately given by the pumping repetition rate). The linear fit in Fig. 2(e) gives the cavity dispersion  $D_2 = 2\pi \times 13.5$  kHz. A separate measurement of the cavity dispersion using a radio-frequency calibrated spectrometer [11] yields  $D_2 = 2\pi \times 11$  kHz (see Supplement 1, Section 1), in reasonable agreement with the linear fit.

## B. Soliton Conversion Efficiency Measurement

The effect of pump pulse repetition rate on efficiency is presented in Fig. 2(e) (red points, right vertical axis). For this measurement, the pump EO comb consisted of 15 comb lines (2 ps pulse), the average pump power was 25 mW, and the cavity loading condition was fixed such that  $Q_{ex}$  was 21 million. However,  $\delta\omega$  was adjusted to maximize soliton power for each repetition rate. The data show that the soliton efficiency (and output power) increases when the

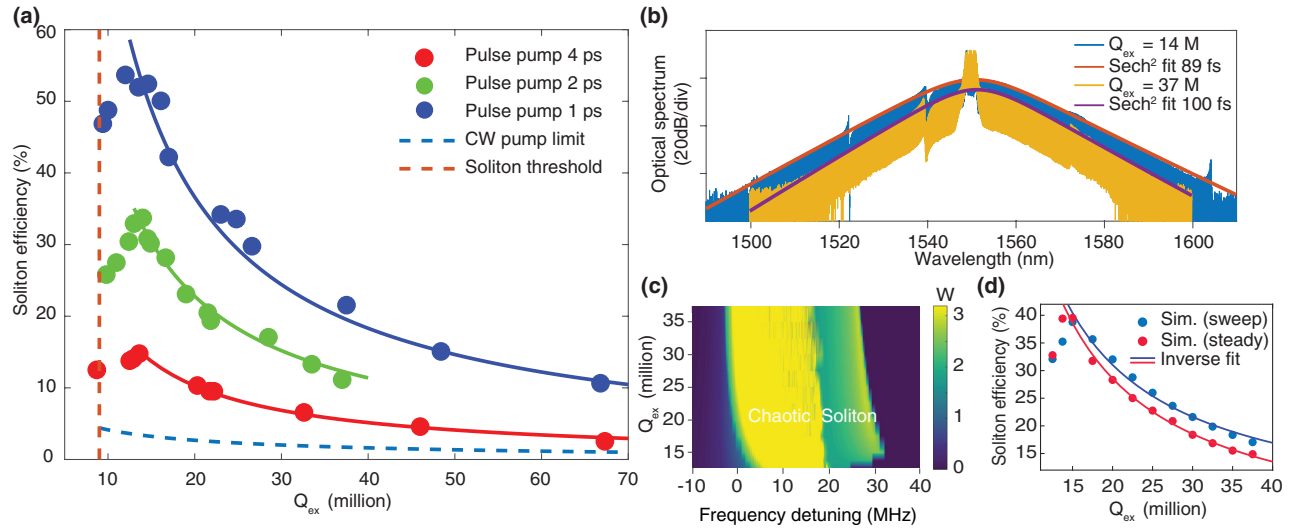


**Fig. 3.** Measurement of soliton efficiency. (a) Measured soliton conversion efficiency versus  $Q_{ex}$  for different numbers of pulse pump comb lines: seven comb lines (red circles, 4 ps FWHM duration), 15 comb lines (green circles, 2 ps FWHM duration), and 31 comb lines (blue circles, 1 ps FWHM duration). The solid curves are inverse  $Q_{ex}$  fits of the measured efficiencies. Pump pulse peak power is the same for all measurements. The blue dashed line is the soliton efficiency under the cw pumping case assuming the maximum detuning limit and the same peak power as the pulse pump case. The red dashed line is the theoretical threshold  $Q_{ex}$  for soliton formation. (b) Optical spectra of pulse pumped soliton microcombs with  $Q_{ex} = 14$  million (blue) and 37 million (yellow). The soliton output power is higher for lower  $Q_{ex}$  with the same pump average power. (c) Color plot of the simulated intracavity soliton power versus detuning and  $Q_{ex}$ . The pulse pump consists of 15 comb lines, the average pump power is 25 mW, and  $Q_0$  is 100 million. The noisy comb regime is plotted at a fixed level of 3.2 W. (d) Simulated soliton conversion efficiency versus  $Q_{ex}$  obtained from (c) when using sweeping  $\delta\omega$  (blue) and steady  $\delta\omega$  (red) in simulations, respectively. The plot optimizes pump detuning  $\delta\omega$  for each  $Q_{ex}$  value, and the contribution from the pump frequencies is excluded when calculating the simulated soliton powers (similar to experimental measurements).

pump pulse repetition rate is reduced, which is consistent with Fig. 1. This phenomenon has also been observed in prior experimental [21] and simulation studies [32] and is attributed to the balance between the de-synchronization (repetition-rate offset) and the Raman-induced drift [32], which leads to a more extended soliton step with higher output power. The scale used for the repetition rates in Fig. 2(e) is relative to the highest drive repetition rate (i.e., 22.112050 GHz) used in the experiment.

The second line of Eq. (4) shows that the efficiency scales nearly inversely with  $Q_{ex}$  when the detuning  $\delta\omega$  is held fixed. To test this dependence, the single-soliton power was measured at a series of  $Q_{ex}$  corresponding to different taper-coupling gap values.  $Q_{ex}$  was determined by measuring the transmission linewidth and relative power transmission on the pumping resonance. The measured single-soliton conversion efficiency (soliton comb power, excluding the pump comb lines, divided by the average power of the input pulse pump) was measured for  $N=7, 15$ , and 31 pump comb lines (effectively 4, 2, and 1 ps pulses), as shown in Fig. 3(a). Average input pump power was set to 54, 25, and 12 mW, respectively, to maintain the same peak power for the pump pulse. [As an aside, if the pump peak power is increased at a fixed  $\xi$  and  $Q_{ex}$  in Eq. (4), the efficiency ultimately decreases since  $\xi_0(0)$  increases.] The following maximum single-soliton conversion efficiencies are measured: 54% ( $N=31$ ) when  $Q_{ex} = 12$  million; 34% ( $N=15$ ) when  $Q_{ex} = 14$  million; and 15% ( $N=7$ ) when  $Q_{ex} = 13.6$  million. Note that the soliton with 54% efficiency was measured with a scanning laser and was not stabilized. The pumping pulse repetition rate was held fixed in each measurement. However, the detuning frequency  $\delta\omega$  was increased slightly as  $Q_{ex}$  was decreased so as to maximize soliton power (and efficiency) at each loading condition. This overall detuning change resulted in

the soliton pulse width changing slightly from 100 fs at  $Q_{ex} = 37$  million to 89 fs at  $Q_{ex} = 14$  million, as obtained by fitting to the soliton spectra [see example in Fig. 3(b) corresponding to 2 ps pump pulses or 15 comb lines in pump]. Since the soliton pulse width is given by  $\tau_s = \sqrt{D_2/(2D_1^2\delta\omega)}$ , the actual variation in  $\delta\omega$  during these measurements was modest. This is further verified through a reasonably good inverse  $Q_{ex}$  fit to data, as provided by the solid colored curves in Fig. 3(a). As an aside, the decreasing efficiency for the lowest  $Q_{ex}$  values coincided with decreasing soliton power versus pump detuning [e.g., see Fig. 2(b) for  $Q_{ex} = 9.8$  M]. Under normal power locking conditions, this would have required reversing the sign of the servo loop for stable operation. Instead, the efficiencies were inferred from the step scan, itself.

A lower bound on  $Q_{ex}$  can be derived by considering the soliton generation criterion noted above [i.e.,  $P(t_s) > 8\sqrt{3}P_{th}/\pi^2$ ]. Making the approximation of temporal alignment of the soliton with the pumping pulse, the corresponding threshold  $Q_{ex}$  is nine million [dashed vertical red line in Fig. 3(a)]. Even though the formula is derived for continuous pumping conditions, there is reasonable agreement with the measured lower bound on  $Q_{ex}$ .

Simulations based on the generalized LLE provide additional confirmation of these measurements (see Supplement 1, Section 2 for details). A pulse driving waveform and a de-synchronization term representing the repetition-rate offset between the pump pulse and the cavity free-spectral-range were used [32]. The 2D color plot in Fig. 3(c) shows soliton power versus  $Q_{ex}$  and  $\delta\omega$ . Simulation parameters are intrinsic  $Q$  factor = 100 million, EO comb lines = 15, average pulse pump power = 25 mW, and pump pulse repetition-rate offset =  $-28.6$  kHz relative to the cavity free-spectral-range. The color map corresponds to average circulating power, and the green region in the plot corresponds to the

soliton step. Within the step, circulating soliton power is relatively constant versus  $\delta\omega$  for  $Q_{\text{ex}} > 15$  million with the exception of a narrow band (yellow band within green step), where soliton power increases slightly. This increase corresponds to temporal alignment of the soliton and pump pulses as discussed above. At the lowest  $Q_{\text{ex}}$  values, soliton steps shorten and soliton power decreases.

Using the simulated maximum circulating soliton power, the maximum output power is calculated (excluding the pump lines) and used to calculate the efficiency in Fig. 3(d). Both a steady-state and swept efficiency are plotted. The latter is evaluated when the soliton position transiently coincides with the pump pulse maximum and is therefore consistently larger than the steady-state case. A maximum efficiency of 39% is reached at  $Q_{\text{ex}} = 15$  million. At this point, both the swept and steady-state results converge since the soliton is able to stably align with the pumping maximum for this lower  $Q_{\text{ex}}$  value. The efficiency decrease at the lowest  $Q_{\text{ex}}$  (less than 10 million) is also reproduced. Since power carried by the pump frequencies was excluded in calculating the experimental and numerical efficiency, this exclusion can cause the observed efficiency reduction, as the comb bandwidth becomes narrower with very low  $Q_{\text{ex}}$ .

The measured efficiencies are also consistent with the approximate values given by Eq. (8). However, to make a comparison between this expression and measurement, it is necessary to add back the pumping power within the  $\text{sech}^2$  envelope to the measurement. For example, the microcomb generated in Fig. 3(b) with  $Q_{\text{ex}} = 14$  million has a 3 dB bandwidth of 2 THz (pump bandwidth is about 0.3 THz), and the experimental conversion efficiency is 34%, while Eq. (8) gives an efficiency of 46%. By fitting the soliton envelope and adding back the pump lines power removed by filtration of the pump, we arrive at an experimental efficiency of 43%, which is in reasonable agreement with Eq. (8).

### C. Soliton and Pump Pulse Delay Measurement

Here, the temporal delay of the pump and soliton pulses are measured using a balanced optical cross-correlator (BOC), as shown in Fig. 2(a). While a temporal delay was observed for solitons generated in a free-space enhancement cavity [41], the dependence of this delay on pump conditions has not been experimentally studied yet, especially in the presence of broad Raman gain, such as in silica microcavities. At the same time, the above analyses have shown that this delay is critical to the soliton pumping efficiency under pulse pumping. For this measurement, a portion of the pumping pulse was coupled and used as a timing reference. The BOC converts the delay change between the soliton and pumping pulse into a voltage signal [42,43]. Figure 4(a) shows the measured relative delay change versus soliton pulse width (pump detuning  $\delta\omega$ ). Note that the absolute relative delay could not be measured due to the difficulty in calibrating the absolute zero delay accurately. The soliton moves about 600 fs (about six times the soliton pulse width) when varying the detuning under the 2 ps pump pulse. The relative delay was also observed to change with varying pump power for a fixed soliton power, as shown in Fig. 4(b). In the experiment, to obtain a wider tuning range in the soliton trapping position, a slightly chirped pump pulse is used [22,23].

Analytical and simulated results are also included in Fig. 4. Since only relative delay was measured, these were shifted vertically to align with the measurements. The specific regime studied here corresponds to Fig. 1(c) (red markers, higher  $Q_{\text{ex}} = 34$  M), and the pump rate is more negatively detuned. Also, for consistency

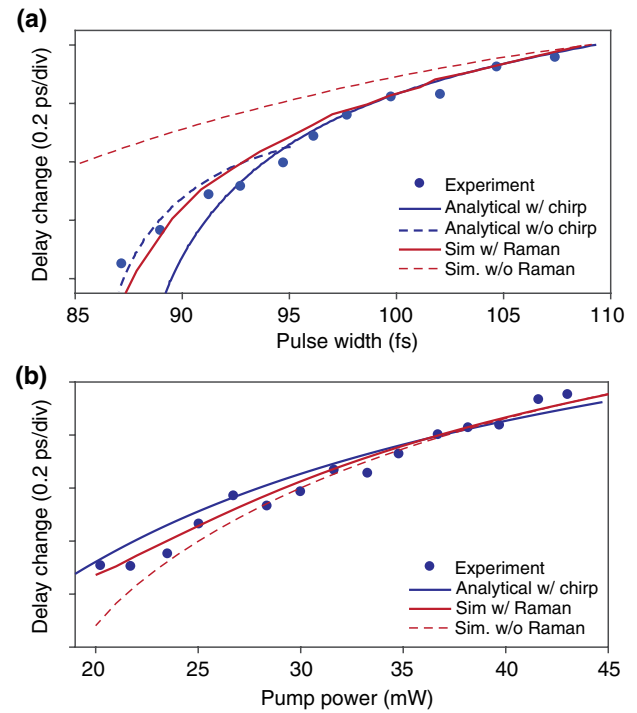


**Fig. 4.** Relative temporal delay between the pump pulse and the soliton. (a) Measured and theoretical (analytical and simulated) relative delay change between the soliton and pumping pulse when changing the detuning  $\delta\omega$  (plotted as soliton pulse width). (b) Measured and theoretical (analytical and simulated) relative delay change with varying pump power.

with the experiments, the analytical and simulated results in Fig. 4 include a modest amount of chirping in the pump pulse, which was used to fit the data. To provide comparison, an unchirped analytical trace is included in Fig. 4(a) (dashed blue curve). As can be seen (and noted above), chirping extends the pulse width range (equivalently detuning  $\delta\omega$ ) over which solitons exist. Specifically, solitons that are longer than 95 fs do not exist for the unchirped case. But, otherwise, the chirping does not dramatically alter the behavior. The presence of the Raman effect, on the other hand, can be seen to have a significant impact on the relative delay versus tuning. Specific parameters used in the simulated and analytical results are provided in Supplement 1, Sections 2 and 3.

## 4. SUMMARY

A closed form expression for pulse pumping efficiency was developed using the Lagrangian method and compared with experiment and simulation [Eq. (4)]. Motion of a soliton under a pulsed pump is shown to obey a generalized Adler equation [Eq. (5)]. The efficiency expression for cw pumping [Eq. (1)] showcases the challenge of operating microcombs at low repetition rates [11]. Pulse pumping enables a tradeoff, wherein low-rate operation is facilitated by the added complexity of pumping pulse generation. Beyond this, pulse pumping introduces new features into the soliton step (i.e., power versus pump detuning). Depending upon the pumping repetition rate relative to the cavity round-trip rate, the step can feature extrema that occur interior to the step. Moreover, in the overloaded case, the soliton power monotonically decreases with increasing detuning. These behaviors are in contrast to cw pumping, where soliton power monotonically increases with pump detuning. Likewise, the Raman process creates a complex

relationship between the soliton position relative to the pumping field maximum. The resulting motion of the soliton relative to the pumping pulse under various tuning and pump power conditions was measured. Efficiency is maximum when using a strongly over-coupled resonator, and record high efficiency was demonstrated. Overall, the presented experimental and theoretical results show how pulse pumped solitons can be optimized to improve the efficiency of microcomb systems. They also provide new insights on soliton dynamics in coherently pumped cavities under pulse pumping conditions.

**Funding.** National Aeronautics and Space Administration (80NM0018 D0004); Air Force Office of Scientific Research (FA9550-18-1-0353); National Science Foundation (1908231).

**Acknowledgment.** We thank Anan Dai, Kemal Safak, and Franz X. Kärtner for building the BOC, as well as Andrei Vladimirov at Weierstrass Institute for discussions on modeling.

**Disclosures.** The authors declare no conflicts of interest.

**Data availability.** Data underlying the results presented in this paper are not publicly available at this time but may be obtained from the authors upon reasonable request.

**Supplemental document.** See Supplement 1 for supporting content.

<sup>†</sup>These authors contributed equally to this paper.

## REFERENCES

1. T. Herr, V. Brasch, J. D. Jost, C. Y. Wang, N. M. Kondratiev, M. L. Gorodetsky, and T. J. Kippenberg, "Temporal solitons in optical microresonators," *Nat. Photonics* **8**, 145–152 (2014).
2. T. J. Kippenberg, A. L. Gaeta, M. Lipson, and M. L. Gorodetsky, "Dissipative Kerr solitons in optical microresonators," *Science* **361**, eaan8083 (2018).
3. D. T. Spencer, T. Drake, T. C. Briles, J. Stone, L. C. Sinclair, C. Fredrick, Q. Li, D. Westly, B. R. Ilic, A. Bluestone, N. Volet, T. Komljenovic, L. Chang, S. H. Lee, D. Y. Oh, M.-G. Suh, K. Y. Yang, M. H. P. Pfeiffer, T. J. Kippenberg, E. Norberg, L. Theogarajan, K. Vahala, N. R. Newbury, K. Srinivasan, J. E. Bowers, S. A. Diddams, and S. B. Papp, "An integrated-photonics optical-frequency synthesizer," *Nature* **557**, 81–85 (2018).
4. M.-G. Suh, Q.-F. Yang, K. Y. Yang, X. Yi, and K. J. Vahala, "Microresonator soliton dual-comb spectroscopy," *Science* **354**, 600–603 (2016).
5. A. Dutt, C. Joshi, X. Ji, J. Cardenas, Y. Okawachi, K. Luke, A. L. Gaeta, and M. Lipson, "On-chip dual-comb source for spectroscopy," *Sci. Adv.* **4**, e1701858 (2018).
6. M.-G. Suh, X. Yi, Y.-H. Lai, S. Leifer, I. S. Grudinin, G. Vasisht, E. C. Martin, M. P. Fitzgerald, G. Doppmann, J. Wang, D. Mawet, S. B. Papp, S. A. Diddams, C. Beichman, and K. Vahala, "Searching for exoplanets using a microresonator astrocomb," *Nat. Photonics* **13**, 25–30 (2019).
7. E. Obrzud, M. Rainer, A. Harutyunyan, M. H. Anderson, J. Liu, M. Geiselmann, B. Chazelas, S. Kundermann, S. Lecomte, M. Cecconi, A. Ghedina, E. Molinari, F. Pepe, F. Wildi, F. Bouchy, T. J. Kippenberg, and T. Herr, "A microphotonic astrocomb," *Nat. Photonics* **13**, 31–35 (2019).
8. P. Marin-Palomo, J. N. Kemal, M. Karpov, A. Kordts, J. Pfeifle, M. H. Pfeiffer, P. Trocha, S. Wolf, V. Brasch, M. H. Anderson, R. Rosenberger, K. Vijayan, W. Freude, T. J. Kippenberg, and C. Koos, "Microresonator-based solitons for massively parallel coherent optical communications," *Nature* **546**, 274–279 (2017).
9. M. Mazur, M.-G. Suh, A. Fülöp, J. Schröder, V. Torres-Company, M. Karlsson, K. J. Vahala, and P. A. Andrekson, "High spectral efficiency coherent superchannel transmission with soliton microcombs," *J. Lightwave Technol.* **39**, 4367–4373 (2021).
10. C. Bao, L. Zhang, A. Matsko, Y. Yan, Z. Zhao, G. Xie, A. M. Agarwal, L. C. Kimerling, J. Michel, L. Maleki, and A. E. Willner, "Nonlinear conversion efficiency in Kerr frequency comb generation," *Opt. Lett.* **39**, 6126–6129 (2014).
11. X. Yi, Q.-F. Yang, K. Y. Yang, M.-G. Suh, and K. Vahala, "Soliton frequency comb at microwave rates in a high-Q silica microresonator," *Optica* **2**, 1078–1085 (2015).
12. P.-H. Wang, J. A. Jaramillo-Villegas, Y. Xuan, X. Xue, C. Bao, D. E. Leaird, M. Qi, and A. M. Weiner, "Intracavity characterization of micro-comb generation in the single-soliton regime," *Opt. Express* **24**, 10890–10897 (2016).
13. J. K. Jang, Y. Okawachi, Y. Zhao, X. Ji, C. Joshi, M. Lipson, and A. L. Gaeta, "Conversion efficiency of soliton Kerr combs," *Opt. Lett.* **46**, 3657–3660 (2021).
14. X. Yi, Q.-F. Yang, K. Y. Yang, and K. Vahala, "Theory and measurement of the soliton self-frequency shift and efficiency in optical microcavities," *Opt. Lett.* **41**, 3419–3422 (2016).
15. X. Xue, P.-H. Wang, Y. Xuan, M. Qi, and A. M. Weiner, "Microresonator Kerr frequency combs with high conversion efficiency," *Laser Photon. Rev.* **11**, 1600276 (2017).
16. A. Fülöp, M. Mazur, A. Lorences-Riesgo, Ó. B. Helgason, P.-H. Wang, Y. Xuan, D. E. Leaird, M. Qi, P. A. Andrekson, A. M. Weiner, and V. Torres-Company, "High-order coherent communications using mode-locked dark-pulse Kerr combs from microresonators," *Nat. Commun.* **9**, 1598 (2018).
17. B. Y. Kim, Y. Okawachi, J. K. Jang, M. Yu, X. Ji, Y. Zhao, C. Joshi, M. Lipson, and A. L. Gaeta, "Turn-key, high-efficiency Kerr comb source," *Opt. Lett.* **44**, 4475–4478 (2019).
18. Ó. B. Helgason, F. R. Arteaga-Sierra, Z. Ye, K. Twayana, P. A. Andrekson, M. Karlsson, J. Schröder, and V. Torres-Company, "Dissipative solitons in photonic molecules," *Nat. Photonics* **15**, 305–310 (2021).
19. X. Xue, X. Zheng, and B. Zhou, "Super-efficient temporal solitons in mutually coupled optical cavities," *Nat. Photonics* **13**, 616–622 (2019).
20. A. W. Bruch, X. Liu, Z. Gong, J. B. Surya, M. Li, C.-L. Zou, and H. Tang, "Pockels soliton microcomb," *Nat. Photonics* **15**, 21–27 (2021).
21. E. Obrzud, S. Lecomte, and T. Herr, "Temporal solitons in microresonators driven by optical pulses," *Nat. Photonics* **11**, 600–607 (2017).
22. M. H. Anderson, R. Bouchand, J. Liu, W. Weng, E. Obrzud, T. Herr, and T. J. Kippenberg, "Photonic chip-based resonant supercontinuum via pulse-driven Kerr microresonator solitons," *Optica* **8**, 771–779 (2021).
23. V. Brasch, E. Obrzud, S. Lecomte, and T. Herr, "Nonlinear filtering of an optical pulse train using dissipative Kerr solitons," *Optica* **6**, 1386–1393 (2019).
24. Y. Xu, Y. Lin, A. Nielsen, I. Hendry, S. Coen, M. Erkintalo, H. Ma, and S. G. Murdoch, "Harmonic and rational harmonic driving of microresonator soliton frequency combs," *Optica* **7**, 940–946 (2020).
25. W. Weng, A. Kaszubowska-Anandarajah, J. He, P. D. Lakshmiyasimha, E. Lucas, J. Liu, P. M. Anandarajah, and T. J. Kippenberg, "Gain-switched semiconductor laser driven soliton microcombs," *Nat. Commun.* **12**, 1425 (2021).
26. S. A. Diddams, K. Vahala, and T. Udem, "Optical frequency combs: coherently uniting the electromagnetic spectrum," *Science* **369**, eaay3676 (2020).
27. I. Hendry, W. Chen, Y. Wang, B. Garbin, J. Javaloyes, G.-L. Oppo, S. Coen, S. G. Murdoch, and M. Erkintalo, "Spontaneous symmetry breaking and trapping of temporal Kerr cavity solitons by pulsed or amplitude-modulated driving fields," *Phys. Rev. A* **97**, 053834 (2018).
28. J. K. Jang, M. Erkintalo, S. Coen, and S. G. Murdoch, "Temporal tweezing of light through the trapping and manipulation of temporal cavity solitons," *Nat. Commun.* **6**, 7370 (2015).
29. H. Lee, T. Chen, J. Li, K. Y. Yang, S. Jeon, O. Painter, and K. J. Vahala, "Chemically etched ultrahigh-Q wedge-resonator on a silicon chip," *Nat. Photonics* **6**, 369–373 (2012).
30. X. Li, B. Shen, H. Wang, K. Y. Yang, X. Yi, Q.-F. Yang, Z. Zhou, and K. Vahala, "Universal isocontours for dissipative Kerr solitons," *Opt. Lett.* **43**, 2567–2570 (2018).
31. P. Bhansali and J. Roychowdhury, "Gen-Adler: the generalized Adler's equation for injection locking analysis in oscillators," in *Asia and South Pacific Design Automation Conference (IEEE, 2009)*, pp. 522–527.
32. I. Hendry, B. Garbin, S. G. Murdoch, S. Coen, and M. Erkintalo, "Impact of desynchronization and drift on soliton-based Kerr frequency combs in the presence of pulsed driving fields," *Phys. Rev. A* **100**, 023829 (2019).
33. S. Coen, H. G. Randle, T. Sylvestre, and M. Erkintalo, "Modeling of octave-spanning Kerr frequency combs using a generalized mean-field Lugiato-Lefever model," *Opt. Lett.* **38**, 37–39 (2013).

34. C. Godey, I. V. Balakireva, A. Coillet, and Y. K. Chembo, "Stability analysis of the spatiotemporal Lugiato–Lefever model for Kerr optical frequency combs in the anomalous and normal dispersion regimes," *Phys. Rev. A* **89**, 063814 (2014).
35. M.-G. Suh and K. Vahala, "Gigahertz-repetition-rate soliton microcombs," *Optica* **5**, 65–66 (2018).
36. M. Cai, O. Painter, and K. J. Vahala, "Observation of critical coupling in a fiber taper to a silica-microsphere whispering-gallery mode system," *Phys. Rev. Lett.* **85**, 74–77 (2000).
37. S. M. Spillane, T. J. Kippenberg, O. J. Painter, and K. J. Vahala, "Ideality in a fiber-taper-coupled microresonator system for application to cavity quantum electrodynamics," *Phys. Rev. Lett.* **91**, 043902 (2003).
38. X. Yi, Q.-F. Yang, K. Y. Yang, and K. Vahala, "Active capture and stabilization of temporal solitons in microresonators," *Opt. Lett.* **41**, 2037–2040 (2016).
39. M. Karpov, H. Guo, A. Kordts, V. Brasch, M. H. Pfeiffer, M. Zervas, M. Geiselmann, and T. J. Kippenberg, "Raman self-frequency shift of dissipative Kerr solitons in an optical microresonator," *Phys. Rev. Lett.* **116**, 103902 (2016).
40. C. Bao, Y. Xuan, C. Wang, J. A. Jaramillo-Villegas, D. E. Leaird, M. Qi, and A. M. Weiner, "Soliton repetition rate in a silicon-nitride microresonator," *Opt. Lett.* **42**, 759–762 (2017).
41. N. Lilienfein, C. Hofer, M. Högner, T. Saule, M. Trubetskov, V. Pervak, E. Fill, C. Riek, A. Leitenstorfer, J. Limpert, F. Krausz, and I. Pupeza, "Temporal solitons in free-space femtosecond enhancement cavities," *Nat. Photonics* **13**, 214–218 (2019).
42. J. Kim and F. X. Kärtner, "Attosecond-precision ultrafast photonics," *Laser Photon. Rev.* **4**, 432–456 (2010).
43. C. Bao, M.-G. Suh, B. Shen, K. Şafak, A. Dai, H. Wang, L. Wu, Z. Yuan, Q.-F. Yang, A. B. Matsko, F. X. Kärtner, and K. J. Vahala, "Quantum diffusion of microcavity solitons," *Nat. Phys.* **17**, 462–466 (2021).